PNAS RESEARCH ARTICLE | ENGINEERING

Minimizing the diffusivity difference between vacancies and interstitials in multi-principal element alloys

Bozhao Zhang[a,1], Zhen Zhang[a,b,1], Kaihui Xun[a], Mark Asta[c,d], Jun Ding[a,2], and Evan Ma[a,2]

Edited by Alexis Bell, University of California, Berkeley, CA; received August 17, 2023; accepted December 4, 2023

Interstitial atoms usually diffuse much faster than vacancies, which is often the root cause for the ineffective recombination of point defects in metals under irradiation. Here, via ab initio modeling of single-defect diffusion behavior in the equiatomic NiCoCrFe(Pd) alloy, we demonstrate an alloy design strategy that can reduce the diffusivity difference between the two types of point defects. The two diffusivities become almost equal after substituting the NiCoCrFe base alloy with Pd. The underlying mechanism is that Pd, with a much larger atomic size (hence larger compressibility) than the rest of the constituents, not only heightens the activation energy barrier (E_a) for interstitial motion by narrowing the diffusion channels but simultaneously also reduces E_a for vacancies due to less energy penalty required for bond length change between the initial and the saddle states. Our findings have a broad implication that the dynamics of point defects can be manipulated by taking advantage of the atomic size disparity, to facilitate point-defect annihilation that suppresses void formation and swelling, thereby improving radiation tolerance.

diffusivity | point defects | multi-principal element alloy | irradiation tolerance | local distortion

Significance

Self-interstitials usually move faster than vacancies in metals and conventional alloys by a few orders of magnitude, where such vastly different mobility can have a significant impact on the material's radiation tolerance. In this work, we employ ab initio simulations to add the much larger Pd atoms into NiCoCrFe alloy to form an equiatomic NiCoCrFePd solution, such that the diffusivities of the two types of point defects become very similar in magnitude. Such a matching of vacancy and interstitial diffusion in close-packed materials has not been possible thus far. Our findings suggest strategies of tailoring the dynamics of point defects to suppress void swelling and offer promising means to design irradiation-tolerant alloys for advanced nuclear-energy applications.

Vacancies and interstitials are two types of intrinsic point defects in crystalline materials. It is well known that the self-interstitials (hereafter denoted as "interstitials") usually move much faster than the vacancies in metals. Take pure nickel as an example: at 1,100 K, the vacancy diffusivity is 2×10^{-11} m^2/s, whereas the interstitial diffusivity can reach 1.5×10^{-8} m^2/s, i.e., approximately three orders of magnitude higher (1). One of the notable scenarios where the vastly different mobility of interstitials and vacancies can have a significant impact on material's performance is radiation tolerance. Under irradiation, interstitials and vacancies are generated simultaneously in large numbers inside any material (2–4). In this case, the annihilation of these point defects requires the two types to be in close spatial vicinity, such that they have adequate opportunities to meet and recombine. When the fast-moving interstitials quickly run away, ample vacancies would be left behind, which would then condense to nucleate damage and cause swelling (e.g., stacking fault tetrahedra, dislocation loops, and voids) (4–11).

A previous study (4) has shown that by tailoring the motion of interstitial defect clusters from a long-range one-dimensional mode to a short-range three-dimensional (3D) mode, one can effectively enhance the radiation tolerance of Ni-containing concentrated solid solution alloys, leading to a reduction of void formation by two orders of magnitude at elevated temperatures. Recent studies (2, 12–16) have also demonstrated enhanced irradiation tolerance in multi-principal element alloys (MPEAs, also called high-entropy alloys, HEAs) when compared with traditional dilute alloys and elemental metals. The origin of this improved irradiation resistance is that the migration energy barrier (E_a) of interstitials and vacancies now each take a wide range of values (17) because the migrating defects are now surrounded by a variety of different local atomic environments (4, 18, 19) in the concentrated solution that is inevitably non-uniform in chemical concentration, local chemical order, and lattice distortion. Consequently, the two E_a distributions overlap across a range of values, over which the mobilities of the two types of defects become comparable (17).

Building upon this success with HEAs, it would be desirable to advance design guidelines to develop such concentrated solid solutions featuring diminished diffusivity differences between interstitials and vacancies. Such materials could display an unprecedented propensity for the irradiation-induced point defects to recombine and annihilate. In this work, we propose such a strategy to achieve almost identical diffusion coefficients for interstitials and vacancies, an ideal scenario that has never been realized before in metals and alloys. Using ab initio simulations based on density functional theory (DFT), we find that, with much larger Pd atoms added into the NiCoCrFe base HEA to form an equiatomic NiCoCrFePd solution, interstitial diffusion is slowed down while vacancy motion

Author affiliations: [a]Center for Alloy Innovation and Design, State Key Laboratory for Mechanical Behavior of Materials, Xi'an Jiaotong University, Xi'an 710049, China; [b]Department of Physics, College of Mathematics and Physics, Chengdu University of Technology, Chengdu 610059, China; [c]Materials Sciences Division, Lawrence Berkeley National Laboratory, Berkeley, CA 94720; and [d]Department of Materials Science and Engineering, University of California, Berkeley, CA 94720

Author contributions: J.D. designed research; B.Z. and Z.Z. performed research; K.X. contributed new reagents/analytic tools; M.A., J.D., and E.M. analyzed data; and B.Z., M.A., J.D., and E.M. wrote the paper.

The authors declare no competing interest.

This article is a PNAS Direct Submission.

[1]B.Z. and Z.Z. contributed equally to this work.

[2]To whom correspondence may be addressed. Email: dingsn@xjtu.edu.cn or maen@xjtu.edu.cn.

Published January 24, 2024.

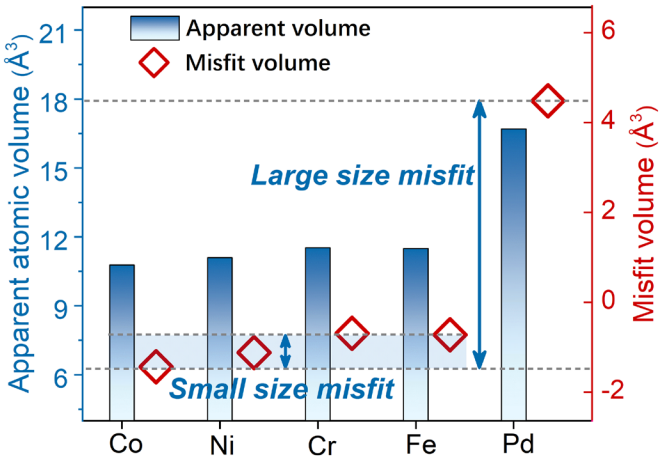

Fig. 1. Atomic volume of each element in NiCoCrFePd alloy. The misfit volume ΔV_n and the apparent atomic volume $V_{apparent}$, of each constituent element. The blue arrows indicate the maximum and minimum differences in ΔV_n among components.

is sped up, both happening in the same material, such that the diffusivities of the two types of point defects become very similar in magnitude.

Results

Atomic Size Misfit in NiCoCrFe and NiCoCrFePd HEAs. The constituent elements in the NiCoCrFe base alloy are neighboring *3d* transition metals in the periodic table and hence of similar atomic size. The alloy is therefore characterized by a small atomic misfit volume for each (type-*n*) and every element, ΔV_n, which can be quantified using (20)

$$\Delta V_n = \sum_m c_m \langle \Delta V^{n/m} \rangle . \quad [1]$$

Here, $\langle \Delta V^{n/m} \rangle$ is the atomic volume change caused by substituting a type-*m* atom with a type-*n* atom and c_m is the fraction of type-*m* atoms, and the brackets express averaging over many different such replacements where the atom of interest has different surrounding atomic environments. This is a conceptual description. Operationally, we consider a random alloy with N^{tot} atoms and total volume V_0^{tot} at the alloy composition. We then add ΔN_n type-*n* atoms by replacing $\Delta N_m = -\Delta N_n c_m/(1-c_n)$ type-*m* atoms for all $m \neq n$ at randomly chosen type-*m* atom sites in the alloy matrix. The volume of the new random alloy is $V^{tot} = V_0^{tot} + \sum_m (-\Delta N_m)\langle \Delta V^{n/m} \rangle$. The average atomic volume $V = V^{tot}/N^{tot}$ can then be expressed as $V = V_0 + \Delta V_n X_s$, with $X_s = \Delta N_n / \left(N^{tot}(1-c_n)\right)$.

Fig. 1 shows that the ΔV_n of Ni, Co, Cr, and Fe are similar, with the largest difference among them being only 0.74 Å^3. A direct consequence of partially replacing Ni, Co, Cr, or Fe with the much larger Pd is the change in atomic misfit volume.As seen in Fig. 1, the largest difference in ΔV_n now increases to 5.92 Å^3. Furthermore, we present in Fig. 1 the apparent atomic volume of each alloying element, $V_{apparent} = V_{avg} + \Delta V_n$, where V_{avg} denotes the average atomic volume. Clearly, the apparent atomic volume of Pd is considerably larger than that of the other elements. As we will see later, the diffusion behavior of point defects will be significantly different before and after Pd substitution.

Mobility of Vacancies versus Interstitials. We next characterize the diffusion behavior of the point defects to establish the link between defect kinetics and the degree of misfit in atomic size. Supercells containing a single vacancy or interstitial were thermalized at a given temperature (below the corresponding melting temperature of the sample to maintain the crystalline structure), and the atomic trajectories were tracked. Then, the atomic mean square displacement (MSD) was calculated by averaging over different time windows in the trajectories. More details are given in *Methods*.

To demonstrate the distinctly different defect kinetics in the two alloys, we present in Fig. 2 the MSD and the real-space trajectories of the defect motion at 1,500 K as an example. In the NiCoCrFe base alloy, the interstitial moves much faster than the vacancy, as manifested by the significantly larger MSD (and thus larger slope in Fig. 2*A*) of the interstitial with respect to that of the vacancy. By introducing Pd, the MSD of the interstitial decreases by a large margin, while that of the vacancy increases drastically, resulting in comparable MSD (and thus diffusivities) of the two types of point defects. The mechanism responsible for this behavior will be discussed later.

Further evidence for the atomic-size-induced change in defect kinetics is shown in Fig. 2 *B*–*E*, which depict the 3D diffusion trajectories of interstitials and vacancies in the two alloys. For the

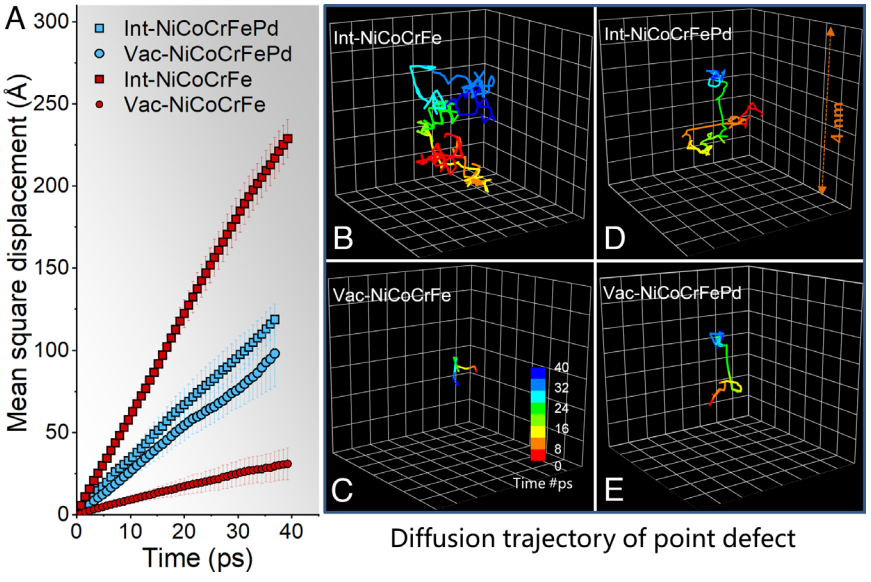

Fig. 2. Point defect diffusion behavior at 1,500 K. (*A*) Comparison of atomic MSD of interstitial and vacancy defects in NiCoCrFe and NiCoCrFePd, averaged over four independent samples. Trajectory of a representative (*B*) interstitial and (*C*) vacancy in NiCoCrFe, over a total time span of 40 ps, compared with their counterpart in NiCoCrFePd, (*D*) and (*E*).

base alloy NiCoCrFe, panels (*B* and *C*), one sees that over a time span of 40 ps, the trajectory of the interstitial is more complex than that of the vacancy. One also recognizes that the total trajectory length and diffusion distance of the former are much larger than those of the latter. These 3D jumps are a result of the defects taking tortuous pathways as they select preferable sites to jump into, given the large variety of local atomic environments surrounding them in a concentrated solution (4, 21–23). The trajectories of the defects in the Pd-substituted system show notable differences from the NiCoCrFe case described above; the paths traveled by the interstitial and vacancy are shorter and longer, respectively, relative to those in the base alloy. Specifically, the NiCoCrFe alloy yields an interstitial trajectory length of 82.5 ± 4.9 nm and a vacancy trajectory length of 2.6 ± 0.7 nm within 40 ps. In contrast, the total trajectory lengths for interstitial and vacancy in NiCoCrFePd alloys are 60.6 ± 10.2 nm and 14.2 ± 1.0 nm, respectively. In other words, the addition of Pd slows down the interstitial jumps but accelerates the motion of vacancies, bringing the two rates close to each other, as seen in Fig. 2*A*.

The tracer diffusion coefficients (D^*) (see *Methods* for calculation details) of the point defects at various temperatures are plotted in Fig. 3, from which the activation energy (E_a) and the pre-exponential factors (D_0) for diffusion of the point defects can be obtained by fitting the data using the Arrhenius law. For the NiCoCrFe alloy, panel (*A*), the diffusivity of the interstitial is on average one order of magnitude larger than that of the vacancy, consistent with the findings of previous studies (24). Remarkably, upon substitution with the larger Pd, panel (*B*), this difference in diffusivity is diminished to nearly zero, achieving an almost equal mobility for the vacancy and the interstitial. This result thus contrasts with the long-accepted norm that the diffusivities of vacancies and interstitials in metals and alloys differ by at least one order of magnitude (25, 26). Also seen in Fig. 3 is that the E_a of interstitial diffusion in the NiCoCrFe alloy is significantly smaller than that of vacancy diffusion, whereas the E_a of the two types of point defects become almost equal (the difference is within the range of error) in the case of the Pd-substituted alloy. Apparently, the change in E_a is the origin of the changed diffusivity behavior.

In Fig. 4, we compare the diffusivities of vacancies and interstitials as obtained from our ab initio Molecular Dynamics (AIMD) calculations and those documented in previous studies (24, 27–30). One observes that the NiCoCrFePd alloy investigated in this work yields the smallest difference in activation energy between the two types of defects when compared with some representative *fcc* pure metals and conventional alloys. This result indicates that adding a concentrated constituent with larger size is by far the most effective in closing the gap between the diffusivities of vacancies and interstitials. This strategy holds promise in developing irradiation-resistant materials for which a similar mobility of vacancies and interstitials is desired for a high probability of defect recombination and annihilation, as mentioned earlier.

Further evidence for the pronounced influence of atomic size on defect mobility was obtained from DFT-based climbing image nudged elastic band (CI-NEB) calculations at 0 K for vacancy diffusion migration barrier (Fig. 5) in the Pd-substituted alloy. To contrast to the barrier for the large element Pd undergoing vacancy diffusion, Ni was used to represent the behavior of the small elements in this figure. We first point out that in the concentrated alloys, the migrating atoms are subject to different local chemical environments, such that the migration barriers for both Ni and Pd jumping into vacancies show a wide distribution (as indicated by the error bar–statistical SD). We find that the mean value of the migration barrier for the Ni case is 1.24 eV, which is much larger than the value of 0.91 eV for the Pd case. This result thus supports the observation from our AIMD calculations (Figs. 3 and 4), i.e., the large Pd atom encounters a lower migration barrier (hence higher mobility) than the small (Ni) atoms in vacancy diffusion.

Atomic-Scale Mechanisms of Point Defect Behavior. We consider next the mechanisms that are responsible for the diffusion of point defects in the two alloys we studied. To this end, we performed Wigner-Seitz defect analysis to locate the atomic sites that correspond to vacancies and interstitials and followed their trajectories of motion. The jump probabilities of vacancies and interstitials of different atomic types were then calculated; more details for the analysis are given in *Methods*. Here, the question of primary concern is whether defect migration energy barrier depends on the size of the diffusing species when the migrating atom moves via the vacancy mechanism versus the interstitial mechanism. If the answer is yes, what is the atomic-level origin of this size dependence?

Fig. 6*A* shows that in the base alloy the interstitial jump probability is not very different for the four species. The same can be said for jumps through vacancies, Fig. 6*B*. As we have shown earlier, the NiCoCrFe alloy is characterized by a small atomic size misfit among its constituents. In contrast to the base alloy, after the incorporation of Pd, we observe a clear contrast between the small atomic species (Ni, Co, Fe, Cr) and the larger Pd. From Fig. 6*C* for interstitial diffusion, the small atoms dominate, while Pd rarely participates in jumping events. This happens because

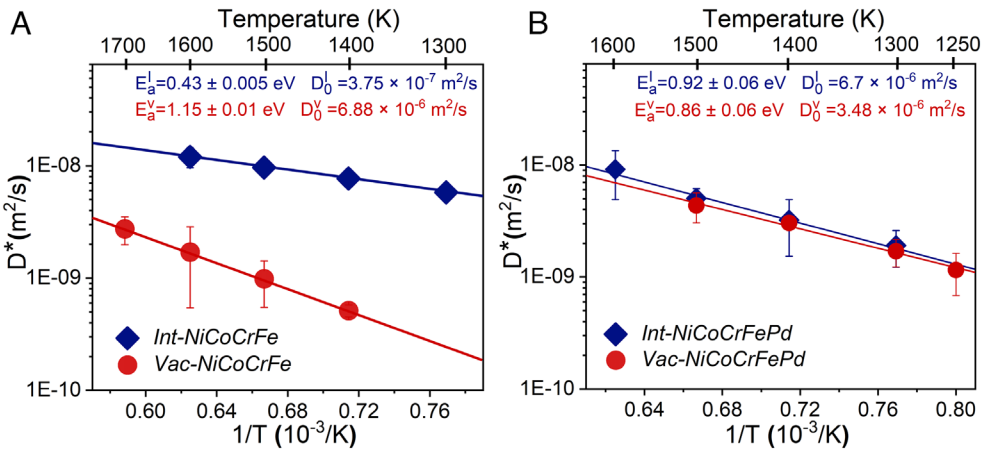

Fig. 3. The tracer diffusion coefficients (D^*) of vacancies and interstitials in (*A*) NiCoCrFe and (*B*) NiCoCrFePd as a function of temperature. The activation energies E_a and pre-exponential factors D_0 for vacancy and interstitial are also labeled. The results are based on statistical averaging of four independent samples calculated in AIMD simulations, and the error bars are the SEs of D^*. Note that some markers hide the error bars in the Figures.

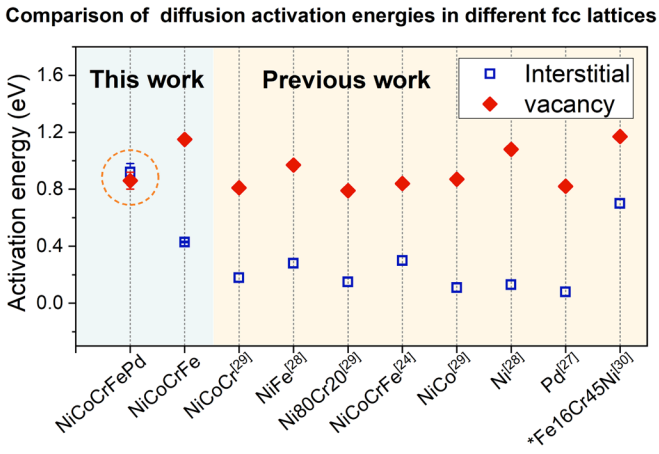

Fig. 4. Comparison of interstitial and vacancy activation energies between our simulation results and other *fcc* metals/alloys reported in previous studies. Labels with and without * represent experimental and computational data, respectively. The superscript number after each of the composition labels on the *x* axis indicate corresponding reference numbers. The NiCoCrFePd alloy yields the smallest difference between the vacancy and interstitial activation energies.

the interstitial pairs move in the form of dumbbells (31, 32) and dumbbells involving large Pd can hardly form and move. The large-sized Pd is expected to cost more energy when displaced from the lattice site to become interstitial (dumbbell).

The case for vacancy diffusion is shown in Fig. 6*D*. The Pd exhibits considerably larger mobility than the small atom, when migrating via vacancies, which is generally consistent with the previous work (33). It is perhaps unexpected that the large Pd atom facilitates vacancy migration, to the extent that the jump rate of Pd becomes manyfold faster than the base elements. To help understand this intriguing observation, Fig. 7 analyzes what transpires on the atomic level, upon the migration of a vacancy in the two alloys we contrast in this study. The atoms selected for our analysis are those involved in the migration of the vacancy, including a Ni (or a Pd) atom, labeled as atom #1 that jumps into the vacancy, and four surrounding atoms (labeled as *s* atoms) that are nearest neighbors of both the vacancy and atom #1; see Fig. 7*A* for a schematic illustration of the local atomic configuration considered. This lattice distortion is given by the distance, Δd_{LD}, deviating from the perfect lattice site after structural relaxation

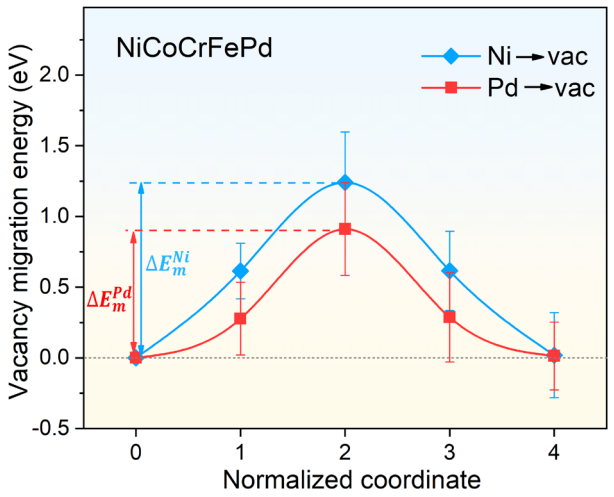

Fig. 5. Comparison of the energy barriers for the migration of a Ni and Pd atom from a lattice site to an adjacent vacancy site in the NiCoCrFePd alloy. The *x*-axis indicates the five equally spaced intermediate positions (with 0 being the initial position) along a selected path of migration in the NEB calculation.

(*Methods*). The average value of this Δd_{LD} for the four *s* atoms, as seen in Fig. 7*C*, is 0.11 Å when atom #1 is Ni, but increases to 0.13 Å when atom #1 becomes Pd. This result is expected, as the four *s* atoms would experience noticeably more displacements, when the atom #1 pushing on them is the much larger Pd compared with the smaller Ni. By contrast, we find that the local lattice distortion of atom #1 is much smaller and insensitive to its size, because this atom is fully encircled by 12 neighboring atoms with no vacant site.

At the first glance, the lattice distortion data would suggest that Pd hopping would be more energy costly than Ni. However, what actually matters in determining the activation energy barrier is not merely the elastic displacement imposed on the atoms at the saddle state but the increase in energy relative to the initial state. We therefore examine the change in the average bond length, Δd, between the two states, i.e., $\Delta d = d_{initial} - d_{saddle}$. Here, d is the average length of the bond between atom #1 and its adjacent *s* atom. Fig. 7*D* displays the distribution of the Ni–*s* and the Pd–*s* bonds in the initial state. Pd–*s* shows a larger $d_{initial}$ (2.59 Å) compared to Ni–*s* (2.54 Å). Upon squeezing atom #1 into the saddle state, as presented in Fig. 7*E*, Δd = 0.111 Å when atom #1 is Pd (resulting in a d_{saddle} = 2.479 Å), significantly smaller than that for a Ni migration event Δd = 0.157 Å (resulting in a d_{saddle} = 2.383 Å). In other words, Pd migration entails less bond compression strain (4.3%) compared with the Ni case (6.2%).

Pd, being placed in a site with atomic volume smaller than it prefers, is under compression and thus in a higher energy state. One can understand the above results as follows: while there is smaller strain on Ni–*s* when Ni is atom #1, when Pd is atom #1, the Pd–*s* initial configuration is elastically compressed to begin with and hence already in a state of elevated energy. The subsequent squeezing of the Pd atom through the saddle point requires less additional compression of the bond length, compared to the case for Ni migration. The energy increase, relative to the initial state, is therefore less for Pd going to the saddle point, when compared with Ni at the same point. Here, the energy penalty is assumed to be controlled by the elastic strain incurred. Actually, when the elastic modulus is factored into the energy consideration, it also favors the compression of Pd–*s*, as the larger Pd with more outer electron shells has a smaller modulus (and higher compressibility) than the Ni–*s* bond [a similar line of thought was discussed in a prior first-principles study, which reported that larger transition metal solutes can actually move faster than smaller atoms in a host Ni lattice (34)]. The picture above provides a structural basis for explaining why a Pd atom jumping to a neighboring vacant site encounters a smaller energy barrier than a smaller Ni atom doing the same (Fig. 5).

Discussions

A reduction in the difference of the diffusivities for vacancies and interstitials has been hypothesized to favor the recombination of annihilation of point defects during early stages of radiation damage. Hence, the NiCoCrFePd alloy is expected to exhibit superior irradiation resistance over the NiCoCrFeMn alloy and other conventional MPEAs that are composed of elements of similar atomic size. Indeed, a recent experimental study (13) on equiatomic NiCoCrFeMn and NiCoCrFePd MPEAs found that alloying with Pd leads to a suppression of the growth of voids and dislocation loops. A strategy has also been reported to introduce additional lattice distortions and chemical heterogeneities using Pd alloying to improve the irradiation resistance of FeCrNiCo-system HEA in cases where irradiation defects are only caused by the aggregation of self-interstitials and vacancies (35). Such an experimental observation aligns well with the predictions in this work that the difference in diffusivities of the interstitials and vacancies would be reduced by the addition of Pd, which is expected to facilitate vacancy-interstitial recombination.

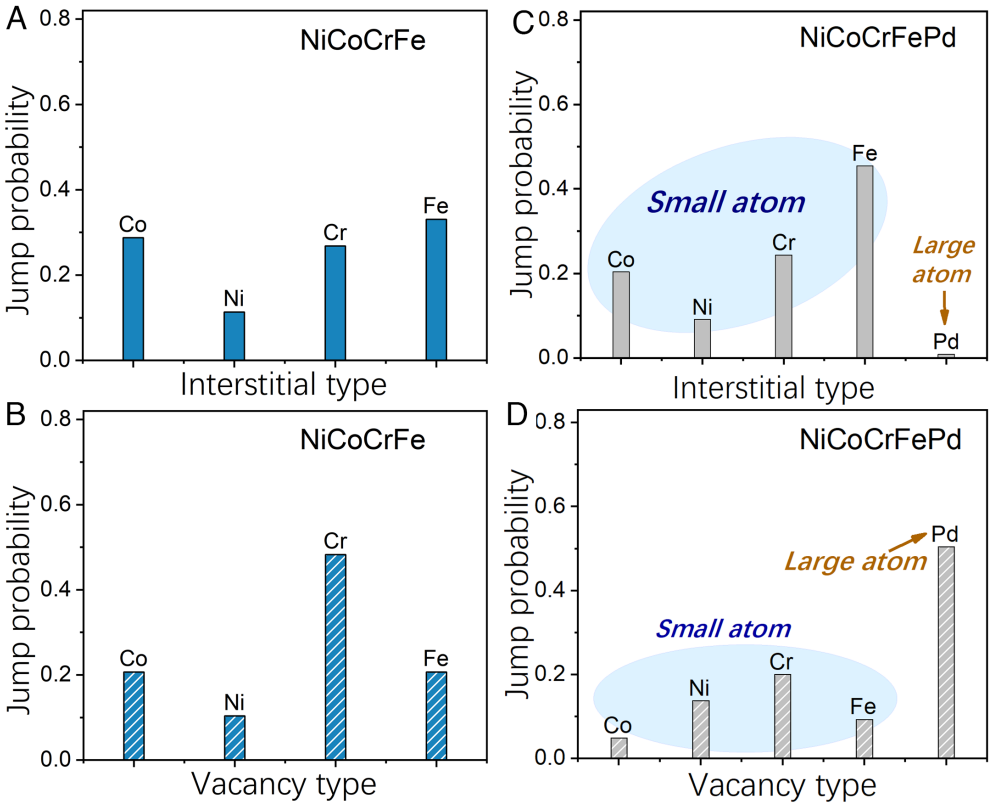

Fig. 6. Jump probability of point defects of various atomic types in the two concentrated solid solution alloys. (*A*) Interstitials and (*B*) vacancies in the NiCoCrFe alloy, compared with their behavior in the NiCoCrFePd alloy, (*C*) and (*D*). The results are the statistical averages of four independent samples for each alloy at different temperatures calculated using AIMD simulations. The small elements in the Pd-added alloy are shaded in blue.

While Pd is too expensive for practical use, less expensive elements with similarly large size are expected to play the same role in NiCoCrFe-based alloys, which should be examined carefully in future. Moreover, we anticipate that the atomic size effect on diffusivities demonstrated for the NiCoCrFe-based alloys in this paper should be relevant to other concentrated alloys more generally. This is based on the projection that the underlying mechanisms for size-induced effects on migration energy barriers

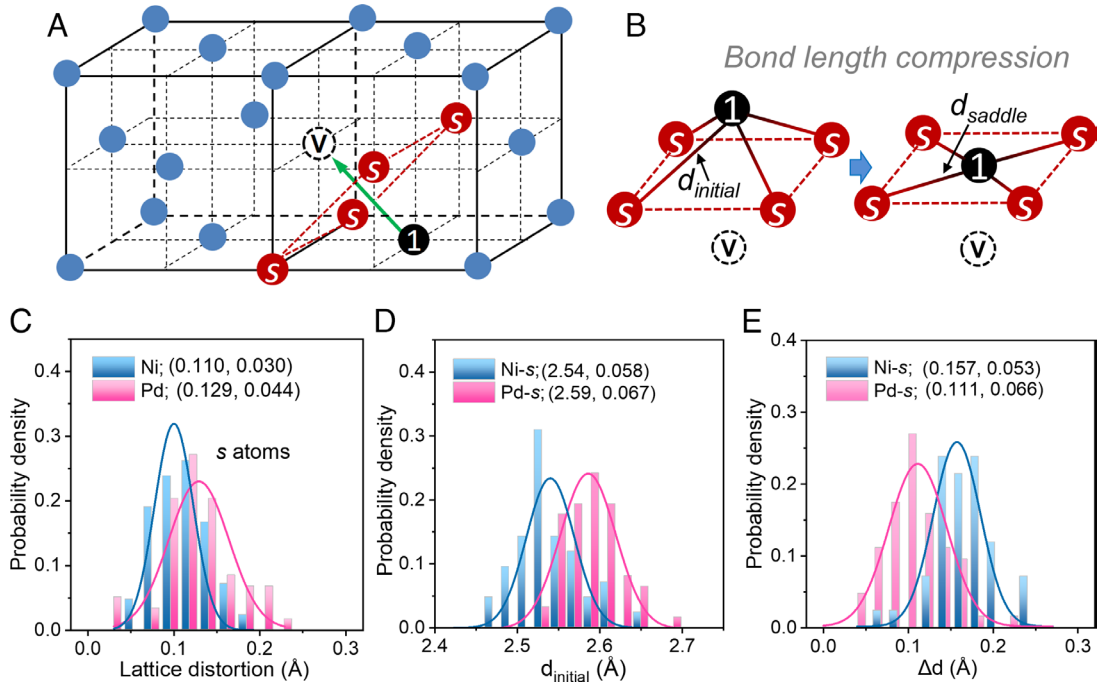

Fig. 7. Local lattice distortion and the change in bond length during vacancy migration in the NiCoCrFePd alloy. (*A*) Schematic illustration of the local atomic configuration around a vacancy. "v" denotes vacancy, "*s*" represents four surrounding nearest-neighboring atoms, and "1" denotes Ni or Pd involved in the vacancy migration. (*B*) Schematic illustration of the change in bond length, Δ*d*, of the "1–*s*" bond, where $\Delta d = d_{initial} - d_{saddle}$. (*C*) Lattice distortion distribution for the four *s* atoms that are nearest neighbors to both the vacancy and atom #1 (Ni versus Pd). (*D*) Distributions of $d_{initial}$ between atom #1 and its adjacent atom in the initial configurations. (*E*) Δ*d* distribution for the Ni–*s* and Pd–*s* bonds. The statistical results are based on 70 independent DFT calculations after energy relaxation. In (*C*–*E*), the numbers in parentheses are the mean and the SD of the distribution, respectively.

discussed in the preceding section should have broad applicability for other species chosen as atom #1- *s*. As such, exploiting the atomic size misfit among the constituent alloying elements may be a general/practical strategy to optimize the element selection in the alloy recipe toward reduced radiation damage. There are also opportunities for further improvement to the irradiation resistance, by tuning the concentration of the constituent species in the alloy. Our results are also expected to be relevant for understanding other phenomena that are closely related to atomic diffusion, such as solid-state phase transformation and compositional segregation in alloys.

Conclusions

By modeling the single-defect diffusion behavior in two NiCoCrFe-based alloys using ab initio simulations, we have demonstrated that concentrated substitutions in an MPEA with a species significantly larger in atomic size than the existing constituents can result in tuning the mobility of interstitials and vacancies, to the point that the two diffusivities become almost equal. Such a matching of vacancy and interstitial diffusion in close-packed metals has not been possible thus far. Adding large Pd atoms into the alloy alters the migration energy barriers of the point defects, leading simultaneously to reduced hopping rates for the interstitials and enhanced migration of the vacancies. The origin of these changes in defect mobilities (and in particular their difference) is that the large atom acts to block the interstitial diffusion channels but at the same time reduces the energy cost for vacancy diffusion through reductions in the bond length compression between the stable and saddle-point states. Our findings suggest strategies to tailor the dynamics of point defects (and consequently the evolution of the microstructure), offering a novel approach to design irradiation-tolerant alloys for advanced nuclear-energy applications.

Methods

AIMD Simulation Details. All AIMD simulations were performed using the DFT-based Vienna Ab Initio Simulations Package (VASP) (36). The generalized gradient approximation due to Perdew–Burke–Ernzerhof (37) was employed to describe the exchange-correlation function and use was made of the projector-augmented wave (38) method. All calculations were performed spin-averaged (i.e., spin-polarization was not taken into account). The initial configurations were generated using special quasi-random structures (SQSs) (39), employing the algorithms in Alloy Theoretic Automated Toolkit (ATAT) code (40). The SQS supercell contained 180 atoms, with atomic arrangements over the sites of the fcc lattice optimized to approximate random configurational disorder. The valence-electron eigenstates were expanded using a plane wave basis set with a cutoff energy of 380 eV. A single k-point (Γ) was used for sampling the Brillouin zone of the supercells. The lattice constants of the initial configurations at different temperature were derived by fitting pressure–volume curves to ensure that the total pressure is maintained roughly near 0 (41) and then the supercell volume was fixed in the following AIMD simulations. To simulate the tracer diffusion behaviors of point defects, we randomly inserted a single vacancy and interstitial dumbbell into the lattice site in different configurations. Additionally, all simulations were statistically averaged over four independent SQS samples to estimate and reduce statistical uncertainties associated with the AIMD data. The simulations were performed at a desired temperature. A simulation time of 50 ps is found to be sufficient to collect reliable diffusion data. The time step was set to 2 fs. We extracted diffusion coefficients, D^*, by applying the "trajectory time decomposition" method (42) to the atomic MSD, as described below. The activation energy E_a was obtained by fitting the Arrhenius law to the temperature-dependent diffusivities.

Estimating Diffusion Coefficients. The defect trajectories of interstitial atoms and vacancy migration in two alloys (i.e., *fcc* NiCoCrFe and NiCoCrFePd) were obtained from AIMD trajectories at a given temperature. The atomic MSD is given by:

$$< R_k^2(t) > = \frac{1}{N_S} \sum_{k=1}^{N_S} \left[\overrightarrow{R_k}(t) - \overrightarrow{R_k}(0) \right]^2. \quad [2]$$

Here, $\overrightarrow{R_k}(t)$ represents the position of atom k at time t averaged over the time origin. N_S is the number of atoms of species s. One can obtain the tracer diffusion coefficients of all atoms (D^*) or a specific species s (D_s^*) by means of linear fitting of the time-dependent MSD of all atoms, or all atoms of a particular species (s), using the Einstein relation (43):

$$D^* = \frac{< R_k^2(t) >}{2nt}. \quad [3]$$

Here, n is the dimensionality, and $n = 3$ is chosen in these simulations since we observed 3D diffusion of interstitials and vacancies.

The tracer diffusion coefficient D^* calculated by Eq. **2** was normalized in terms of the interstitial or vacancy concentration. The activation energy E_a and pre-exponential factor D_0 can be estimated by fitting the temperature-dependent diffusion coefficient using the Arrhenius law:

$$D^* = D_0 \exp\left(\frac{-E_a}{K_B T} \right). \quad [4]$$

Estimating Defect Jump Probabilities. We first extracted the point defect trajectory via Wigner–Seitz defect analysis as implemented in Open Visualization Tool (OVITO) (44). Then, by taking into account the jump probability p_{i-j} of i-related dumbbells, the interstitial jump probabilities p_i^{Int} of elements i of interest were calculated as:

$$p_i^{Int} = \frac{1}{2} \sum_{i \neq j}^{N_d} p_{i-j} + \sum_{i=j}^{N_s} p_{i-j}, \quad [5]$$

where N_d is the dumbbell species with different elements and N_s is the dumbbell species with the same elements in alloys. p_{i-j} denotes the jump probability of dumbbells consisting of elements i and j, which is given by:

$$p_{i-j} = \frac{n_{i-j}}{\sum_{i-j}^{N} n_{i-j}}. \quad [6]$$

Here, n_{i-j} is the number of interstitial dumbbells consisting of elements i and j extracted by a single defect trajectory. N represents the total dumbbell species of alloys. Since vacancy migration is a jumping event involving a single element, the vacancy jump probability p_i^{Vac} can then be calculated as

$$p_i^{Vac} = \frac{n_i}{\sum_i^N n_i}. \quad [7]$$

Here, n_i is the number of jumping vacancies of element i. N denotes the vacancy species in alloys.

All the diffusion data were derived from statistical averaging of four independent samples for each alloy at different temperatures.

CI-NEB Calculations. We performed DFT-based CI-NEB calculations (45) at 0 K. 3 × 3 × 3 NiCoCrFePd supercells (108 atoms) were used in calculations of the energy barriers of a single Ni or Pd atom migrating to an adjacent vacancy. A total of 80 independent NEB pathways with different atomic environments were assembled to statistically average the migration energy. CI-NEB calculations were performed using the VASP package with a plane wave cutoff energy of 350 eV. The ionic forces of the initial and final configurations were first relaxed to <2 meV/Å, and the energy criterion in each SCF iteration was set to 1×10^{-4} eV. Spin polarization was included in all of these NEB calculations, and Brillouin-zone integrations were performed using 2 × 2 × 2 Monkhorst–Pack meshes. Other details of the calculations are the same as described above for the AIMD simulations. Five equally spaced points along the chosen pathway were sampled during the NEB calculation. The CI-NEB calculation was stopped when the change in maximum atomic force was less than <0.05 meV/Å. Our convergence tests demonstrated that the migration energies obtained by

CI-NEB with the currently adopted computational parameters are within 1% of those calculated with higher precision (i.e., a cutoff energy of 500 eV and 3 × 3 × 3 Monkhorst–Pack meshes).

Local Lattice Distortion. The local lattice distortions, Δd_{LD}, of the atoms in the nearest neighborhood of a vacancy can be calculated as:

$$\Delta d_{LD} = \frac{1}{N}\sum_{i}^{N}\sqrt{(x_i - x_i')^2 + (y_i - y_i')^2 + (z_i - z_i')^2}, \quad [8]$$

where (x_i, y_i, z_i) are the coordinates of atom i at the ideal lattice sites, and (x_i', y_i', z_i') corresponds to its coordinates after lattice relaxation. Here, $N = 4$ is the number of co-neighboring atoms of a vacancy and its adjacent Pd or Ni, and $N = 1$when calculating the local lattice distortions of Pd or Ni itself adjacent to a vacancy. All configurations used to calculate lattice distortion are constructed by randomly generating individual vacancies in the first nearest-neighbor shell adjacent to Pd or Ni in a supercell containing 108 atoms. A total of 70 independent configurations were used for VASP structural relaxations.

Data, Materials, and Software Availability. All study data are included in the main text.

ACKNOWLEDGMENTS. B.Z. and J.D. acknowledge National Key R&D Program of China (Grant No. 2023YFB3712002) and the HPC platform of Xi'an Jiaotong University. J.D. and E.M. are indebted to Xi'an Jiaotong University for hosting their work at the Center for Alloy Innovation and Design. Z.Z. and E.M. acknowledge National Natural Science Foundation of China (Grant No. 52231001). This work is partially supported by the National Natural Science Foundation of China under Grant No. 12075179. M.A. acknowledges the support from the US Department of Energy, Office of Science, Office of Basic Energy Sciences, Materials Sciences and Engineering Division under contract no. DE-AC02-05CH11231, as part of the Damage-Tolerance in Structural Materials (KC13) program, which also supported J.D. during early stages of this research performed at Lawrence Berkeley National Laboratory.

1. K. Ferasat *et al.*, Accelerated kinetic Monte Carlo: A case study; vacancy and dumbbell interstitial diffusion traps in concentrated solid solution alloys. *J. Chem. Phys.* **153**, 074109 (2020).
2. Y. Lin *et al.*, Enhanced radiation tolerance of the Ni-Co-Cr-Fe high-entropy alloy as revealed from primary damage. *Acta Mater.* **196**, 133–143 (2020).
3. M. W. Ullah, D. S. Aidhy, Y. Zhang, W. J. Weber, Damage accumulation in ion-irradiated Ni-based concentrated solid-solution alloys. *Acta Mater.* **109**, 17–22 (2016).
4. C. Lu *et al.*, Enhancing radiation tolerance by controlling defect mobility and migration pathways in multicomponent single-phase alloys. *Nat. Commun.* **7**, 13564 (2016).
5. F. Granberg *et al.*, Mechanism of radiation damage reduction in equiatomic multicomponent single phase alloys. *Phys. Rev. Lett.* **116**, 135504 (2016).
6. Z. Zhang *et al.*, Effect of local chemical order on the irradiation-induced defect evolution in CrCoNi medium-entropy alloy. *Proc. Natl. Acad. Sci. U.S.A.* **120**, e2218673120 (2023).
7. O. El-Atwani *et al.*, Outstanding radiation resistance of tungsten-based high-entropy alloys. *Sci. Adv.* **5**, eaav2002 (2019).
8. X. F. Kong *et al.*, Interface facilitated transformation of voids directly into stacking fault tetrahedra. *Acta Mater.* **188**, 623–634 (2020).
9. K. Y. Yu *et al.*, Removal of stacking-fault tetrahedra by twin boundaries in nanotwinned metals. *Nat. Commun.* **4**, 1377 (2013).
10. X. Zhang *et al.*, Radiation damage in nanostructured materials. *Prog. Mater. Sci.* **96**, 217–321 (2018).
11. D. S. Aidhy *et al.*, Point defect evolution in Ni, NiFe and NiCr alloys from atomistic simulations and irradiation experiments. *Acta Mater.* **99**, 69–76 (2015).
12. Y. H. Lu *et al.*, A promising new class of irradiation tolerant materials: Ti2ZrHfV0. 5Mo0. 2 high-entropy alloy. *J. Mater. Sci. Technol.* **35**, 369–373 (2019).
13. T.-N. Yang *et al.*, Influence of irradiation temperature on void swelling in NiCoFeCrMn and NiCoFeCrPd. *Scripta Mater.* **158**, 57–61 (2019).
14. S. Xia, X. Yang, T. Yang, S. Liu, Y. Zhang, Irradiation resistance in Al x CoCrFeNi high entropy alloys. *JOM* **67**, 2340–2344 (2015).
15. Z. Zhang, D. E. J. Armstrong, P. S. Grant, The effects of irradiation on CrMnFeCoNi high-entropy alloy and its derivatives. *Prog. Mater. Sci.* **123**, 100807 (2022).
16. C. Lu *et al.*, Radiation-induced segregation on defect clusters in single-phase concentrated solid-solution alloys. *Acta Mater.* **127**, 98–107 (2017).
17. S. Zhao, T. Egami, G. M. Stocks, Y. Zhang, Effect of d electrons on defect properties in equiatomic NiCoCr and NiCoFeCr concentrated solid solution alloys. *Phys. Rev. Mater.* **2**, 013602 (2018).
18. O. R. Deluigi *et al.*, Simulations of primary damage in a high entropy alloy: Probing enhanced radiation resistance. *Acta Mater.* **213**, 116951 (2021).
19. Y. Zhang, T. Egami, W. J. Weber, Dissipation of radiation energy in concentrated solid-solution alloys: Unique defect properties and microstructural evolution. *MRS Bull.* **44**, 798–811 (2019).
20. B. Yin, W. A. Curtin, First-principles-based prediction of yield strength in the RhIrPdPtNiCu high-entropy alloy. *npj Comput. Mater.* **5**, 14 (2019).
21. G. Nandipati, W. Setyawan, K. J. Roche, R. J. Kurtz, B. D. Wirth, Effect of confinement of SIA cluster diffusion by impurities on radiation defect accumulation due to 14 MeV neutrons in tungsten. *J. Nucl. Mater.* **542**, 152402 (2020).
22. T. Shi *et al.*, Distinct point defect behaviours in body-centered cubic medium-entropy alloy NbZrTi induced by severe lattice distortion. *Acta Mater.* **229**, 117806 (2022).
23. S. Zhao, Y. Osetsky, A. V. Barashev, Y. Zhang, Frenkel defect recombination in Ni and Ni-containing concentrated solid-solution alloys. *Acta Mater.* **173**, 184–194 (2019).
24. Z. Fan *et al.*, Diffusion-mediated chemical concentration variation and void evolution in ion-irradiated NiCoFeCr high-entropy alloy. *J. Mater. Res.* **36**, 298–310 (2021).
25. J. R. Shoemaker *et al.*, Point defect study of CuTi and CuTi2. *J. Mater. Res.* **6**, 473–482 (1991).
26. C. Lu *et al.*, Direct observation of defect range and evolution in ion-irradiated single crystalline Ni and Ni binary alloys. *Sci. Rep.* **6**, 1–10 (2016).
27. S. Foiles, M. Baskes, M. S. Daw, Embedded-atom-method functions for the fcc metals Cu, Ag, Au, Ni, Pd, Pt, and their alloys. *Phys. Rev. B* **33**, 7983 (1986).
28. Y. N. Osetsky, L. K. Béland, R. E. Stoller, Specific features of defect and mass transport in concentrated fcc alloys. *Acta Mater.* **115**, 364–371 (2016).
29. S. Zhao, On the role of heterogeneity in concentrated solid-solution alloys in enhancing their irradiation resistance. *J. Mater. Res.* **35**, 1103–1112 (2020).
30. C. Dimitrov, O. Dimitrov, Influence of nickel concentration on point defect migration in high-nickel Fe-Cr-Ni alloys. *J. Nucl. Mater.* **152**, 21–29 (1988).
31. S. Zhao, Y. Osetsky, Y. Zhang, Preferential diffusion in concentrated solid solution alloys: NiFe, NiCo and NiCoCr. *Acta Mater.* **128**, 391–399 (2017).
32. S. Zhao, Defect properties in a VTaCrW equiatomic high entropy alloy (HEA) with the body centered cubic (bcc) structure. *J. Mater. Sci. Technol.* **44**, 133–139 (2020).
33. J. Gao, J. Ding, Y. Zhang, T. Zhu, Q. Yu, Tuning the near room temperature oxidation behavior of high-entropy alloy nanoparticles. *Nano Res.* **15**, 3569–3574 (2022).
34. A. Janotti, M. Krcmar, C. L. Fu, R. C. Reed, Solute diffusion in metals: Larger atoms can move faster. *Phys. Rev. Lett.* **92**, 085901 (2004).
35. S. Shen *et al.*, The design of Pd-containing high-entropy alloys and their hardening behavior under He ion irradiation. *Acta Mater.* **261**, 119404 (2023).
36. G. Kresse, J. Furthmüller, Efficiency of ab-initio total energy calculations for metals and semiconductors using a plane-wave basis set. *Comput. Mater. Sci.* **6**, 15–50 (1996).
37. J. P. Perdew, K. Burke, M. Ernzerhof, Generalized gradient approximation made simple. *Phys. Rev. Lett.* **77**, 3865 (1996).
38. P. E. Blöchl, Projector augmented-wave method. *Phys. Rev. B* **50**, 17953 (1994).
39. A. Zunger, S.-H. Wei, L. Ferreira, J. E. Bernard, Special quasirandom structures. *Phys. Rev. Lett.* **65**, 353 (1990).
40. A. Van De Walle, M. Asta, G. Ceder, The alloy theoretic automated toolkit: A user guide. *Calphad* **26**, 539–553 (2002).
41. F. D. Murnaghan, The compressibility of media under extreme pressures. *Proc. Natl. Acad. Sci. U.S.A.* **30**, 244–247 (1944).
42. N. Anento, A. Serra, Y. N. Osetsky, Atomistic study of multimechanism diffusion by self-interstitial defects in α-Fe. *Model. Simul. Mater. Sci. Eng.* **18**, 025008 (2010).
43. H. Mehrer, *Diffusion in Solids: Fundamentals, Methods, Materials, Diffusion-Controlled Processes* (Springer Science & Business Media, 2007), vol. 155.
44. A. Stukowski, Visualization and analysis of atomistic simulation data with OVITO–the Open Visualization Tool. *Model. Simul. Mater. Sci. Eng.* **18**, 015012 (2010).
45. G. Henkelman, B. P. Uberuaga, H. Jónsson, A climbing image nudged elastic band method for finding saddle points and minimum energy paths. *J. Chem. Phys.* **113**, 9901–9904 (2000).